Atmospheric
Chemistry
and Physics
Discussions

Open Access

Atmospheric polarimetric effects on GNSS Radio Occultations: the ROHP-PAZ field campaign

R. Padullés[1], E. Cardellach[1], M. de la Torre Juárez[2], S. Tomás[1], F. J. Turk[2], S. Oliveras[1], C. O. Ao[2], and A. Rius[1]

[1]Institut de Ciències de l'Espai (ICE – CSIC/IEEC), Barcelona, Spain
[2]NASA Jet Propulsion Laboratory, California Institute of Technology, Pasadena, CA, USA

Correspondence to: R. Padullés (padulles@ice.cat)

ACPD

15, 18747–18785, 2015

ROHP-PAZ field campaign

R. Padullés et al.

Title Page

Abstract	Introduction
Conclusions	References
Tables	Figures

|◄ | ►|
◄ | ►
Back | Close

Full Screen / Esc

Printer-friendly Version

Interactive Discussion

Abstract

This study describes the first experimental observations showing that hydrometeors induce polarimetric signatures in Global Navigation Satellite System (GNSS) signals. This evidence is relevant to the PAZ Low Earth Orbiter, which will test the concept and applications of polarimetric GNSS Radio Occultation (RO) (i.e. ROs obtained with a two-polarization antenna). A ground field campaign was carried out in preparation for PAZ to verify the theoretical sensitivity studies about this concept (Cardellach et al., 2015). The main aim of the campaign is to identify and understand the factors that might affect the polarimetric GNSS observables. Studied for the first time, GNSS signals measured with two polarimetric antennas (H, horizontal and V, vertical) are shown to discriminate heavy rain events, by comparing the measured phase difference between the H and V phase delays ($\Delta\Phi$) in different weather scenarios. The measured phase difference indicates higher dispersion under rain conditions. When individual events are examined, significant increases of $\Delta\Phi$ occur when the radio signals cross rain cells. Moreover, the amplitude of such signal is much higher than the theoretical prediction for precipitation; thus other sources of polarimetric signatures have been explored and identified. Modelling of other hydrometeors like melting particles and ice crystals have been proposed to explain the obtained measurements, with good agreement in more than 90 % of the cases.

1 Introduction

Global Navigation Satellite System (GNSS) Radio Occultations (RO) space-borne missions have been probing the Earth's atmosphere since 1995 (e.g. Rocken et al., 1997). They have been shown to be useful for climate monitoring (e.g. Steiner et al., 2011) and nowadays their thermodynamic profiles are being assimilated operationally into several numerical weather prediction (NWP) models (e.g. Healy et al., 2005; Cucurull and Derber, 2008).

A new measurement concept presented in Cardellach et al. (2015) aims at detecting and quantifying heavy precipitation events using polarimetric GNSS RO, by means of measuring the difference between the phase delays of the horizontal and the vertical components of the received propagated signal. This technique will be tested aboard the PAZ Low Earth Orbiter (LEO) satellite with the RO and Heavy Precipitation experiment (ROHP-PAZ), and it will be the first attempt to detect rain using L band frequencies (1.575 GHz, i.e. $\lambda = 19.03$ cm). The launch is planned for Q3 2015. The theoretical analysis performed in Cardellach et al. (2015) demonstrated not only that heavy rain events could be detected, but also that an approximated vertical structure of the rain cells could be retrieved.

Prior to the launch of the PAZ satellite, a field campaign has been conducted in order to study, for the first time, L1 occulting signals obtained at two polarizations, and start to identify and understand the factors that might affect the polarimetric signal. Placed on top of a mountain peak 1670 m above the mean sea level, the experiment was set up with an engineering model of the PAZ's polarimetric antenna pointing at the horizon and a commercial JAVAD receiver (provided by the German Research Center for Geosciences GFZ), enclosed in a shelter. A zenith-looking geodetic GNSS antenna has also been used for positioning. The RO antenna points south, and it tracks all the visible satellites in the East-West field of view from 0 to 20° of elevation and from 150 to 270° of azimuth (see Fig. 1). Although all the satellites are tracked simultaneously, only those crossing the main beam of the antenna are used in the posterior analysis. These are the identified by the Pseudo-Random Noise (PRN) numbers G10, G14, G15, G22 and G31.

The main objective was to collect a large amount of data free of rain, and to catch some heavy rain events in order to observe differences in the polarimetric observables between the two data sets. The area was chosen specifically for this purpose, given that the region is mainly dry and several intense local Mediterranean storms occur a few times per year (Ducrocq et al., 2014). The experiment ran for 8 months, from 21 March

to 10 October in 2014. During this period, it collected data for about 170 days. There were about 25 days of rain, from which 5 could be considered heavy rain.

The geometry and measurements used for this experiment are closely related to those of the polarimetric weather radar observations. In the radar observations, the differential reflectivity (Z_{dr}) and the specific differential phase (K_{dp}) are the most important polarization signatures for rain characterization at low elevation angles (e.g. Bringi and Chandrasekar, 2001). Some differences apply in our case: we are limited to one single observable, the differential phase between the H- and V-ports phase delay (ΔΦ), defined as:

$$\Delta\Phi = \int_L K_{dp} dl \tag{1}$$

where L is the path length under the influence of K_{dp}. Note also that K_{dp} is here defined in propagation (forward-scattering) rather than back-scattering. This is a one dimensional observation, since it is an integral along the ray path. Furthermore, the weather radars work with frequencies equal or higher than 3 GHz, thus the sensitivity to hydrometeors is expected to be higher than for the L band signals.

From the polarimetric radar observations it is known that different kinds of rain, precipitation and particles could produce different K_{dp}. Studies for rain (e.g. Bringi and Chandrasekar, 2001; Trömel et al., 2013), ice (e.g. Vivekanandan et al., 1994; Ryzhkov and Zrnić, 1998), snow (e.g. Matrosov, 1992; Kennedy and Rutledge, 2011) and melting layer (e.g. Baldini and Gorgucci, 2006; Trömel et al., 2013) characterization using polarimetric observables have been widely conducted, as well as the continuous satellite observation of rain such as the Tropical Rainfall Measurement Mission (TRMM) and the Global Precipitation Mission (GPM) missions.

Therefore, our aim here is not to characterize the different kinds of precipitation or hydrometeors, but to take advantage of this knowledge to understand our observations.

This paper is organized in the following way: in Sect. 2 the experiment geometry and the acquired data are described in detail, and a comparison with the satellite set-

up is performed. Problems with the signal, multipath characterisation, and expected improvements from satellite observations are addressed here. The collocated meteorological data used for validation are described in Sect. 3. The statistical results of the experiment are shown in Sect. 4, and a comparison with the forward model simulation results is performed in Sect. 5. Finally, in Sect. 6 the conclusions are discussed.

2 Polarimetric GNSS data

2.1 Observables

GNSS signal observables are the carrier phase and the pseudorange. In the standard RO, these are measured with a circular co-polar antenna (right-handed, as transmitted signals), and they are used to obtain the bending angle, which in turn is used to obtain the refractivity, pressure and temperature profiles (Kursinski et al., 1997). We refer to these as the standard RO thermodynamic profiles. The geometry found in the experiment is not a common RO configuration. Instead, our receiver is inside the atmosphere, i.e. on the ground, and therefore the tangent point – LEO trajectory is missing (see Fig. 2). The lack of symmetry and the non-existence of negative elevation observations does not allow us to retrieve the standard thermodynamic profiles (Healy et al., 2002), which are going to be retrieved from the satellite in the future experiment.

Also, the fact that the receiver is on the ground means that the radio-link is crossing all the atmosphere layers during all the observation time. In this configuration, the sounding of the atmosphere is different from a RO one. This has an important implication in our observables.

The polarimetric GNSS observable $\Delta\Phi$ is the difference between the the carrier phase delay measured in the Horizontal (H) port and and the one measured in the Vertical (V) port. The observations in the H and V ports of the polarimetric antenna are independent, and therefore the receiver treats them separately. The GNSS receivers keep track of the total phase relative to their initial measurement, but the value asso-

ciated with the first measurement is arbitrary (Blewitt, 1989). In this case, both signals (H and V) suffer from this ambiguity (phase ambiguity, K) in their respective channel:

$$\Phi_i(t) = \rho(t) + \rho_{\text{atm}}(t) + \rho_{\text{hyd}}^i(t) + \rho_{\text{ion}}(t) + m^i(t) + d^i + C(t) + K^i \quad (2)$$

where Φ is the measured carrier phase delay at the i port (H or V). ρ is the geometry range between the satellite and the receiver since the initial measurement (the same for H and V), ρ_{atm} denote the delay due to the neutral atmosphere that is equal in the H and V channels, ρ_{hyd} is the phase delay due to the interaction with hydrometeors (the terms that we are interested in) and ρ_{ion} denote the ionospheric delay. m represents the multipath in each component, the term d refers to the hardware effects of the receiver and the transmitter and C represents the clock drifts and errors. K is the arbitrary initial constant that does not depend on time. Most of these terms are common in both components, thus the phase difference is:

$$\Delta\Phi(t) = \rho_{\text{hyd}}^{\text{H}}(t) - \rho_{\text{hyd}}^{\text{V}}(t) + m + K + d \quad (3)$$

where $m = m^{\text{H}} - m^{\text{V}}$, $K = K^{\text{H}} - K^{\text{V}}$ and $d = d^{\text{H}} - d^{\text{V}}$.

We do not have sufficiently precise L2 measurements to solve the initial phase bias using pseudoranges (as it is done in Blewitt, 1989). This term K changes in every arc of data (continuous tracking) and therefore our observation is not absolute, but relative to the first measurement.

To avoid further problems, we identify the loss of tracks that occur during the tracking of the same PRN, and we separate them in continuous arcs. Every time that the track is lost, the receiver starts again with a new arbitrary constant. For each day, we only consider the longest arc, and discard the rest.

To enable comparison among different observations, we force each arc to have a 0 mean:

$$\Delta\Phi'(t) = \Delta\Phi(t) - \langle\Delta\Phi(t)\rangle. \quad (4)$$

This step homogenizes all the observations, and allows the comparison among them. It removes the contribution from K and d terms, but it also erases any constant signature of the polarimetric measurement. Thus, any rain contribution in which depolarization is present since the beginning and remains until the end of the observation will be missed.

In a satellite to satellite geometry (PAZ scenario), even without knowing the arbitrary initial constants we expect to be able to calibrate the initial phase, since in the beginning of the occultation the radio-link between the GPS and the LEO is not crossing the atmosphere.

2.2 Multipath

Multipath is the result of the combination of the signal from the satellite and one or more signals from the same source that have followed different paths to reach the receiver, for example, being reflected on the ground or on a metallic structure. It affects the phase differently in the H and in the V components, giving a pattern that depends on the surrounding geometry, environmental conditions and position of the transmitter. Our antenna is placed over a shelter, which has several metallic pieces. Also, there is a meteorological station a few meters from the experiment. Thus, our data suffer from a severe multipath. If the reflecting process affected equally both H and V, this effect would cancel in $\Delta\Phi$. However, metallic structures with longitudinal edges might differently affect the scattering in the two polarizations.

In similar environmental conditions, the multipath pattern ought to repeat after a sidereal day (period of the GPS orbits), thus it can be characterized, and to a large extent, removed. We define our observations as $\Delta\Phi_{day}^{PRN}(t)$. This corresponds to one PRN arc for a specific day. In order to homogenise the samples, we convert time (t) to elevation (ϵ), since the same satellite has to be in the same position (i.e. elevation) after a sidereal day.

In ideal conditions, $\Delta\Phi_{day}^{PRN}(\epsilon)$ should be the same sidereal day after sidereal day. So, to characterize the multipath pattern, we perform the average and the standard

deviation as a function of elevation for a given set of days. We define as *no-rain* days those days when no rain is present in the area, and *rain* days when the radar has detected significant reflectivity (Z) nearby. The multipath pattern (m) and its standard deviation (σ) for *no-rain* days for a certain PRN ($m_{\text{no-rain}}^{\text{PRN}}, \sigma_{\text{no-rain}}^{\text{PRN}}$) can be seen in Fig. 3 top. Usually, $\sigma_{\text{no-rain}}^{\text{PRN}}$ is large at low elevations. This is due to a lower quality of the signal, that has travelled through longer atmosphere layers than those rays at higher elevations.

To obtain the final measurement, i.e. the one that will be analysed, this multipath pattern is removed from the measured signal $\Delta\Phi'(\epsilon)$:

$$\Delta\Phi_{\text{day}}^{\text{PRN}}(\epsilon)\Big|_{\text{corrected}} = \Delta\Phi_{\text{day}}^{\text{PRN}}(\epsilon)\Big|_{\text{observed}} - m_{\text{no-rain}}^{\text{PRN}}(\epsilon). \tag{5}$$

The antenna pattern is also affecting the measurements differently in each component. Its effect, though, is implicitly taken into account in the $m_{\text{no-rain}}^{\text{PRN}}$ term, and therefore it is implicitly corrected applying Eq. (5).

Hereafter, the corrected measurement will be referred as $\Delta\Phi_{\text{day}}^{\text{PRN}}(\epsilon)$. An example of corrected $\Delta\Phi_{\text{day}}^{\text{PRN}}$ is given in Fig. 3 bottom.

2.3 Ionosphere

It is well known that the ionosphere affects the GPS signal carrier phase delays and pseudorranges. In terms of polarization, there are two effects that have an effect on the signals:

Faraday rotation changes the polarization axis of the propagating signals, proportionally to the total electron content (TEC) crossed and the Earth magnetic field. Yet, the rotation angle effect is the same in both components, H and V, and therefore it should not be noticeable when differentiating both signals.

On the other hand, the Cotton-Mouton effect could induce different phase delays in each component (e.g. Zhang et al., 2010). However, the effect is expected to be small enough to be negligible.

A summary of the expected differences between the spaceborne mission and this ground experiment can be found in Table 1.

3   Meteorological weather data

The objective of our analysis is to understand the new polarimetric observations, which requires collocated meteorological information. We have been provided by the data from the weather radars of the area, data from the METEOSAT satellites and data from radiosondes.

The Servei Meteorològic de Catalunya (METEOCAT) has a weather radar network covering the Catalan coastal area (Bech et al., 2004). We have access to the data from one of the radars, which has full coverage of the area under study. These radars are all Doppler systems, with one single polarization, operating at C-band (5.6 GHz). The provided data consists of the radar reflectivity (Z) in dBZ, as a function of latitude, longitude and height. Its resolution is 1 km × 1 km × 1 km in a grid of 300 km × 300 km, per 10 km of height, and every 6 min. Since it is not a polarimetric radar, we can not extract information such as K_{dp} or Z_{dr}, which would provide clues about the orientation of the particles.

METEOCAT has also a network of ground stations that provides the accumulated precipitation, temperature and relative humidity in 30 min batches. One of them is a few meters from our antenna. In a radius of 30 kms, there are 4 more ground stations. Through them we can have an approximation of the surface rain rate during the rain events.

Besides the radar and ground stations data, Cloud Type (CTY), Cloud top Phase (CP) and Cloud Top Height (CTH) data products from the Support to Nowcasting and Very Short Range Forecasting (NWC-SAF) have been used. The data have been provided by the Agencia Estatal de Meteorología (AEMET) and the European Organisation for the Exploitation of Meteorological Satellites (EUMETSAT). These data results from

the combination of satellite imagery and Numerical Weather Prediction (NWP) inputs. It is available for the study area every 15 min.

Using the CTY and CP products we can know the cloud top phase and using the CTH product we can know the height of the top of the cloud. Combining this information we can properly collocate our observations. Unfortunately, these sets of data do not provide information about the orientation of the ice particles. Only those with its major axis oriented horizontally would induce a positive polarimetric signature.

To complement all the information we use the measurements provided by METEO-CAT's radiosondes. These radiosondes are launched two times per day (00:00 and 12:00 UTC) at a distance of approximately 50 km to the South-East of our antenna, and provide temperature, pressure and humidity as a function of height. Even though the temporal resolution is not very high, approximated temperature and refractivity vertical profiles are obtained interpolating both radiosondes, weighting their information with the time difference.

Once all the information is recompiled, we can perform an exact collocation of the observations with the weather data. To do so, we first simulate the rays from the GPS to the antenna using a ray-tracer called OAT, which solves the trajectory of each ray across the atmosphere characterized by the retrieved refractivity profiles (Aparicio and Rius, 2004). An illustration of the performed collocation can be seen in Fig. 4. Then, we interpolate all the weather information for each of the points of the ray trajectory. For this analysis, each ray consists of 500 points, separated ~ 0.52 km among them. We simulate 501 rays, between 0 and $20°$ of elevation.

4 Statistical results: Do rain induce polarimetric features?

4.1 Standard deviations

Once the data have been pre-processed as described in Sect. 2, the analysis should determine whether the corrected $\Delta\Phi_{\text{day}}^{\text{PRN}}(\epsilon)$ is affected by rain or not.

First of all, an analysis of the standard deviation is performed. To do so, corrected $\Delta\Phi_{day}^{PRN}$ are grouped in three sub-sets. For each sub-set the standard deviation as a function of elevation $\sigma_{subset}^{PRN}(\epsilon)$ is computed:

– Dry days: days when the observation was made in a low relative humidity conditions (i.e. the relative humidity has not reached 100 %) and without rain ($\sigma_{dry}^{PRN}(\epsilon)$).

– Wet days: days either with hight relative humidity (i.e. the relative humidity has reached 100 %) during or before the observation; or rain before or after the observation; or both ($\sigma_{wet}^{PRN}(\epsilon)$).

– Rain days: Days with rain in the surroundings during the observation time ($\sigma_{rain}^{PRN}(\epsilon)$).

This classification has been done in order to compare different environmental situations. For example, high relative humidity conditions could have caused condensation, leading to a wet soil and different multipath and antenna behaviour. The results of σ averaged for all elevation angles, for several PRNs and for the three day sub-sets are summarized in Table 2.

It can be seen that *dry* days present always a lower σ than the rest, and that *rain* days exhibit the largest σ. The standard deviation for *wet* days is also larger than for *dry* days, but the difference is less significant than for the *rain* days. There should not be any significant differences between *wet* and *rain* days, in terms of the surroundings condition. For example, just after rain, the soil should be as wet as during the rain. Therefore, the largest σ that *rain* days show could mean that under rain conditions, the signal is affected by something else than for different multipath.

Hereafter and for the rest of the analysis, the correction is done as described in Eq. (5) using the *dry* and *wet* days defined here to calculate $m_{no\text{-}rain}^{PRN}$.

4.2 Phase difference as a function of elevation

Examining each event individually, more features can be observed. To do such analysis, we compare each observation $\Delta\Phi_{day}^{PRN}(\epsilon)$ with the $\sigma_{no\text{-}rain}^{PRN}(\epsilon)$. We define a $2\sigma_{no\text{-}rain}^{PRN}$ threshold to detect polarimetric signatures in the signal: statistically speaking, $\sim 95\,\%$ of the data should be within $\pm 2\sigma_{no\text{-}rain}^{PRN}$. Thus the remaining $5\,\%$ of the data points and those affected by some polarimetric feature should lay beyond $\pm 2\sigma_{no\text{-}rain}^{PRN}$.

Lacking an absolute reference for the phase difference and to identify points overpassing the $\pm 2\sigma_{no\text{-}rain}^{PRN}(\epsilon)$ threshold, we find the elevation point where the difference between $\Delta\Phi_{day}^{PRN}(\epsilon)$ and $-2\sigma_{no\text{-}rain}(\epsilon)$ is minimum, and we identify it as ϵ_{min}. Then, we subtract this difference from the observation, and what we obtain is the observation aligned in a way that for each event its minimum lays on the line of $-2\sigma_{no\text{-}rain}$ threshold:

$$\Delta\Phi_S(\epsilon) = \Delta\Phi(\epsilon) - (\Delta\Phi(\epsilon_{min}) - 2\sigma_{no\text{-}rain}(\epsilon_{min})) \tag{6}$$

After this correction, we can easily detect the points outside the 2σ threshold. The region of $\Delta\Phi_S(\epsilon)$ above the $+2\sigma_{no\text{-}rain}$ threshold is defined as follows:

$$\Delta\Phi_+(\epsilon) = \begin{cases} \Delta\Phi_S(\epsilon) - 2\sigma(\epsilon) & \text{if} \quad \Delta\Phi_S(\epsilon) > 2\sigma(\epsilon) \\ 0 & \text{if} \quad \Delta\Phi_S(\epsilon) \leq 2\sigma(\epsilon) \end{cases} \tag{7}$$

And the area of $\Delta\Phi_+(\epsilon)$ is defined as A_Φ:

$$A_\Phi = \int \Delta\Phi_+(\epsilon)\mathrm{d}\epsilon \tag{8}$$

An example of $\Delta\Phi_S(\epsilon)$ and A_Φ is shown in the bottom plot in Fig. 5. In this procedure, we only consider the option of positive phase differences, as it is expected for rain effects (Cardellach et al., 2015).

We have found 28 observations with $A_\Phi > 0$, of which $82\,\%$ correspond to rainy scenarios. This represents the first experimental confirmation of the theory that precipitation conditions induce polarimetric features in GNSS signals.

5 Are the observed polarimetric features consistent with the models?

In order to explain the observations, forward scattering calculations have been performed. The aim is to simulate the effect of several kinds of hydrometeors, such as rain drops, pristine ice particles and melting ice particles, to cross-compare with weather radar reflectivities, satellite observations and the phase differences measured.

First of all, the K_{dp} and the radar reflectivity factor (Z_e) have been calculated for each hydrometeor type. These calculations have been done using the DDScat code (Draine and Flatau, 1994, 2013).

DDScat provides the phase lag efficiency factor (Q_{pha}) for each polarimetric component H and V. It is related to the forward scattering amplitude f_{sca} through $Q_{pha} = \frac{2\pi}{k} \frac{\Re\{f_{sca}\}}{\pi a_{eff}^2}$. Thus, it can be used to calculate the K_{dp}:

$$K_{dp} = \frac{\lambda}{2\pi} \int \left(Q_{pha}^{H} - Q_{pha}^{V} \right) \pi a_{eff}^2 N(D)\, dD \tag{9}$$

where a_{eff} is the equivolumetric radius of the particle, $N(D)$ is the particle size distribution, D is the equivolumetric diameter and K_{dp} is in $mm\,km^{-1}$.

DDScat also provides the differential backscattering cross section normalized by πa_{eff}^2:

$$Q_{bk} = \frac{1}{\pi a_{eff}^2} \frac{\partial \sigma_{bk}}{\partial \Omega} \bigg|_{\Theta=180} \tag{10}$$

The backscattering cross section can then be obtained:

$$\sigma_{bk} = 4\pi Q_{bk} \pi a_{eff}^2 \tag{11}$$

Using the σ_{bk} we can calculate the radar reflectivity factor Z_e as follows:

$$Z_e = \frac{\lambda^4}{\pi^5 |K_w|^2} \int_0^{D_{max}} \sigma_{bk}(D) N(D)\, dD \tag{12}$$

where λ is the wavelength, K_w is $(m_w^2 - 1)/(m_w^2 + 2)$ and m_w is the complex refractive index of water (Smith, 1984).

K_{dp} is calculated for L band frequency (GNSS observations), and Z_e for C-band frequency (weather radar observations). The reason is that we want to relate the reflectivity obtained by the meteorological weather radar, that operates at C-band, with our observations.

The $N(D)$ that has been used is a gamma function of the form:

$$N(D) = N_0 D^\mu e^{-\Lambda D} \tag{13}$$

where N_0 is the scale parameter, Λ is the slope parameter and μ is the shape parameter (Ulbrich, 1983). These are the 3 parameters of the gamma $N(D)$. The particle size distribution determines other quantities through its moments, such as the K_{dp} (e.g. Eq. 9), Z_e (e.g. Eq. 12), liquid or ice water content (LWC, IWC), effective particle diameter (D_{eff}), mean weighted diameter (D_m) and rain rate (R). Further details of the relation between these magnitudes and the moments of $N(D)$ can be found in the literature, for example in Williams et al. (2014).

Since there is not a unique parameterization of the $N(D)$ that apply to all scenarios, we generate a set of mathematically valid $(N_0, \Lambda, \mu)^i$ triplets, each one producing a different $N(D)^i$. Then, each triplet has an associated physical magnitude:

$$(N_0, \Lambda, \mu)^i \rightarrow N(D)^i \rightarrow (K_{dp}^i, Z_e^i, \mathrm{LWC}^i, D_{eff}^i, D_m^i, R^i, \ldots)$$

Depending on the hydrometeor being modelled, not all $N(D)$ parameters will be physically consistent, that is, fall in ranges that have been observed amongst various ground validation data (Williams et al., 2014). In the next section we describe the selection criteria for the valid ranges to choose among the possible $N(D)^i$.

5.1 Modelled A_Φ: rain effect

At the beginning of the campaign, only rain was expected to affect the polarimetric signal. To simulate the polarimetric rain effect, the Q_{pha} and σ_{bk} have been calculated

Printer-friendly Version

Interactive Discussion

with DDScat using the predetermined oblate spheroid shapes, with D ranging from 0.1 to 6 mm, and Axis Ratio (AR) following the Beard and Chuang (BC) relation (Beard and Chuang, 1987), as it was done in Cardellach et al. (2015). Shape is sketched in Fig. 6 (left). Some constraints have been applied to the (N_0, Λ, μ) triplets in order to use only those producing physically valid quantities: we have limited R to be as high as 70 mm h^{-1} because the observations from the meteorological ground stations suggest so, and we have limited the LWC to be smaller than 3 g m^{-3}, as an upper limit that is in agreement with the observation of severe storms described in Black and Hallett (2012). All the parameter triplets producing quantities out of these ranges are discarded.

From the chosen $N(D)$ we derive Z_e and K_{dp}. All the valid Z_e^i and K_{dp}^i for rain conditions are shown in black in Fig. 7. To relate the observations from the weather radar and the measurements from the polarimetric antenna, we need to use a Z_e–K_{dp} relation. It can be seen in Fig. 7 how a wide range of possible K_{dp} can be related to a given Z_e. For simplicity, we will use the Z_e–K_{dp} indicated with a thick line in Fig. 7.

We have simulated the expected A_Φ caused by rain for every GNSS measurements, using the radar Z_e values interpolated to GNSS ray trajectories, and this Z_e–K_{dp} relation. The results can be seen in black dots in Fig. 8. Despite the polarimetric signatures happening on rainy days, Fig. 8 shows that rain drops alone do not induce the large polarimetric signals observed. Therefore, the effects of other hydrometeors must be taken into account.

5.2 Could ice and melting particles explain the large polarimetric signatures?

To simulate the ice particles, dendritic shapes have been used. Their characteristics are described in Liu (2008). For melting ice particles, two concentric ellipsoids have been used: the inner one made of pristine ice and the outer one of water. Both have the same axis ratio, ranging from 0.1 to 0.8, and with D ranging from 0.01 to 6 mm. The water shell is considered to range between a 5 and a 10 % of the volume of the inner core. Their shapes are sketched in Fig. 6 (center and right).

A given ice-induced Z_e can be explained by a diversity of ice particle characterizations, such as different combinations of canting angle, IWC, percentage of horizontally oriented particles with respect to randomly oriented ones, or predominant sizes of the particles, among others. This diversity of ice conditions relate to a diversity of K_{dp}. This means that a given Z_e links to many possible K_{dp} values. Since we want to keep this modelling simplistic to understand the contributions and order of magnitude of the polarimetric effect, and because we do not have ancillary information to properly characterize the ice properties, we have simulated this effect using only horizontally oriented dendrites, with a maximum IWC of $1\,\mathrm{g\,m^{-3}}$. Horizontal orientation is supported by many studies, for example Matrosov and Mace (2012) or Noel and Chepfer (2010). The chosen Z_e^i and K_{dp}^i for ice particles are shown in Fig. 7 in blue, and the Z_e–K_{dp} relation used for ice particles is highlighted with a thick blue line.

Melting ice particles have even a wider range of variability. As can be seen in Fig. 7 (in gray), the possible Z_e^i and K_{dp}^i are widely spread. We have used the Z_e–K_{dp} relation indicated with a gray thick line when accounting for melting ice particles. As for rain and pristine ice, this relation is rather arbitrary, as we do not have the required ancillary ground-truth information to properly characterize these particles, and our goal is to explain, to an order of magnitude, what we have measured.

We have separated the contribution of rain, ice, and melting ice particles according to the temperature. The temperatures are given by the METEOCAT's radiosondes, mentioned in Sect. 3. The radar reflectivity measured at heights with temperatures above $1\,^\circ$C is considered to come from rain. Particles in the range between 1 and $-5\,^\circ$C are assumed to be melting ice particles. Below $-5\,^\circ$C they are assumed to be ice. Ice particles are assumed to be bigger in the range between -5 and $-20\,^\circ$C, because this region is considered to be the maximum dendritic growth zone (Kennedy and Rutledge, 2011).

Above the radar measurements, ice contributions are assumed when the simulated ray intersects with ice regions, according to the combination of the Cloud top Phase and Cloud Top Height products. In this case, the particles are assumed to be smaller.

We assume a thickness of the ice particle layer of about 2 km, in agreement with Noel and Chepfer (2010). The results for the simulated A_Φ taking into account the different hydrometheors are shown in orange in Fig. 8.

A block diagram is shown in Fig. 9 to help the reader follow the steps that lead to the Fig. 8 results. All the data, information and relations used from the data acquisition to the final results are summarized in it.

One can notice how the simulated A_Φ increases significantly using all three hydrometeor types with respect to using only rain. In most of the cases, the simulated A_Φ is larger than the measured one. As we have said, the model that we have used is very simple, and the modelling of ice crystals and melting ice particles has assumed very favourable conditions, like the orientation of the particles without canting angle, or the lack of other kind of particles (i.e. aggregate shaped), which would reduce significantly their contribution to the K_{dp}. Also, the model has been applied with the same Z_e–K_{dp} relation for each hydrometeor type, although every event has its own conditions.

In addition, the contribution to A_Φ due to ice and melting particles is only simulated when the observed $\Delta\Phi_+(\epsilon)$ is positive. The reason is that if there were no measurement of $\Delta\Phi_+(\epsilon)$, there would not be oriented crystals in the ray path, nor a contribution to K_{dp}. The Cloud-Aerosol Lidar and Infrared Pathfinder Satellite Observations (CALIPSO) images show how only some regions of the clouds contain oriented ice crystals. This is consistent with discontinuous positive observations of $\Delta\Phi$, as is observed here. Unfortunately, no collocations were found between CALIPSO and our experiment.

The goal of this exercise has been to check if the measured $\Delta\Phi$ (and therefore A_Φ) can be explained by adding the contribution of these hydrometeors to the rain contribution, that by itself underestimated the polarimetric signatures. The results shown in Fig. 8 confirm that adding other hydrometeors in the model increases A_Φ. The Z_e–K_{dp} relations used favoured high K_{dp} and hence high A_Φ for a given Z_e, which explain why orange dots tend to overestimate A_Φ. Fine tuning of the parameters for each individual observation would be needed in order to reproduce the observations, but this is not our

aim here, nor would it be possible to validate such tuning due to the lack of ancillary independent information.

5.3 Illustration cases

In order to further check the internal consistency of the measurements, we compare several observations for different PRNs in the same day, during the evolution of heavy rain episodes. In this section we analyse three such episodes.

The collocation of the ray trajectories with the radar reflectivity are shown for each day and observation, and superimposed there is the $\Delta\Phi_+$. For clarity purposes, in Fig. 10 we only show one illustrative case and the caption details how to understand the plots. Then, the temporal series of such plots along heavy rain episodes are shown in Figs. 11 and 12.

Figure 11 corresponds to events on 14 June, 22 August and 26 May 2014, respectively.

In the case of 14 June 2014, according to the nearby meteorological ground stations, there were maximum accumulations of rain of 14 mm in 30 min. This corresponds to peaks of R higher than $28\,\mathrm{mm\,h^{-1}}$. It can be seen how positive $\Delta\Phi$ is present mainly when larger amount of Z is accumulated at high altitudes. This is in agreement with the fact that rain alone produces lower polarimetric signatures than the ones detected with the present configuration.

On 22 August 2014, the nearby meteorological ground stations suggest R higher than $55\,\mathrm{mm\,h^{-1}}$ according to the accumulated precipitation over 30 min. As in the previous case, positive $\Delta\Phi$ measurements are observed in the regions where significant Z reaches high altitudes, and where the temperature is around or below $0\,^\circ$C (ice and melting particles).

The last case, on 26 May 2014, there were not such high R peaks, but significant Z is also present at high altitudes, in agreement with the positive $\Delta\Phi$ observations.

Among all the studied cases, more than 90 % can be explained with the combined hydrometeor modelling. An example of these cases which failed to explain the obser-

vations can be seen in Fig. 12, on 09 July 2014. In this case, positive $\Delta\Phi$ measurements can not be associated with any significant reflectivity, nor to ice in the tops of the clouds crossed by the ray. More specifically, the positive $\Delta\Phi$ measured while tracking PRN *G*15 remain unclear, so far.

6   Conclusions

For the first time, GNSS occulting signals have been acquired using a two polarization antenna with the aim of detecting rain. This technique, presented in Cardellach et al. (2015), will be tested from space aboard the PAZ Low Earth Orbiter. If successful, it will be possible to provide rain flags, and potentially information about rain structures, collocated with the standard RO thermodynamic profiles.

The experiment presented here was intended to characterize the phenomena that are actually affecting the polarimetric signatures. It has consisted of comparing the measurements of the polarimetric observable $\Delta\Phi$ under different weather conditions, trying to identify rain signatures. Data from 6 GNSS transmitters on ~ 170 different days have been analysed.

Many challenges have arisen in the data analysis process. Three main issues affect the data: the location of the antenna/receiver (low inside the atmosphere, not proper RO geometry), the phase ambiguity problem (linked to internal processing of the commercial receiver, out of our control), and severe and varying multipath (mostly due to the nearby environment, metallic towers and structures). None of these effects are expected (or not as severely) in the spaceborne mission: regarding the location of the antenna/receiver, the future experiment will be in the space, and therefore outside the atmosphere. Being outside the atmosphere will allow a better calibration of the signals thanks to the scanning geometry: a vertical descent from the outer layers approaching the Earth surface. Thus, at the beginning of the observation there are no depolarizing effects, and it will be possible to define the initial state (calibration of the polarimetric phase measurement). Phase ambiguity will be solved, and absolute measurements will

⏮ | ⏭

◀ | ▶

Back | Close

Full Screen / Esc

Printer-friendly Version

Interactive Discussion

be possible, unlike in this experiment. Also, in the satellite we expect the multipath to be smaller, and most importantly, it will not change with the environmental conditions.

After analysing the data, two main conclusions can be extracted.

In a general view, rain scenarios affect the polarimetric observables. The standard
5   deviation of the mean ΔΦ for *dry*, *wet* and *rain* days have been examined. For environmental reasons (wet soil, increase of the reflectivity, etc.), the σ for *wet* and *rain* days is higher than for *dry* days. However, the increase of the σ_{rain} with respect σ_{dry} is between 20 and the 40 % larger than the increase of σ_{wet} with respect σ_{dry}.

This could empirically answer one of the questions that we were seeking for an
10 answer: Are radio-links crossing rain cells affected by any depolarization affect? And if so, is it detectable? According to the σ behaviour under the different weather and environmental conditions, we can answer that under rain scenarios, the measured ΔΦ suffer from higher variability, and the difference from other scenarios is noticeable.

A more detailed analysis of the $\Delta\Phi(\epsilon)$ has been performed for each individual obser-
15 vation. ΔΦ above the defined 2σ threshold, and the computed A_Φ have been compared with simulated results. Simulated K_{dp} using the collocated radar reflectivity has shown that rain drops induce an effect much lower than our measurements. This indicates that other phenomena are inducing polarimetric signatures too. This is an important point in views to the future analysis of the spaceborne ROHP-PAZ data.
20 Ice crystals and melting ice particles have been added to the modelling, using temperature information and satellite imagery to distinguish between hydrometeors. Simulations of these particles have been kept very simplistic, due to the number of possible parameters involved in the modelling and the lack of information to validate them. Our goal at this stage is to identify the sources of polarimetric signatures. The simulations
25 have shown that, in most of the cases, the measured ΔΦ could be explained by the K_{dp} induced by all possible hydrometeors.

Simulated ΔΦ and A_Φ with all the hydrometeors are usually above the measured values. Fine tuning of the parameters involved in the modelling would be needed in

Printer-friendly Version

Interactive Discussion

order to match the observations, but we feel that this would be too speculative and impossible to validate in this particular experiment.

Microphysical analysis of the precipitation and inversion procedures development are left for later studies with RO, data more suitable than mountain-top occultations. Yet, the results obtained here represent the first empirical evidence that hydrometeors induce measurable polarimetric signatures in occulting GNSS signals after the theoretical analysis in Cardellach et al. (2015). These results are helping us to understand the types of processes affecting the data from the future polarimetric RO experiment aboard PAZ. They additionally show the potential capability of polarimetric RO to sense complex precipitable structures, information that will be provided along with thermodynamic profiles and increase the applications of the RO technique.

Title Page

Abstract | Introduction

Conclusions | References

Tables | Figures

◄◄ | ►►

◄ | ►

Back | Close

Full Screen / Esc

Printer-friendly Version

Interactive Discussion

References

Aparicio, J. M. and Rius, A.: A raytracing inversion procedure for the extraction of the atmospheric refractivity from GNSS travel-time data, Phys. Chem. Earth A/B/C, 29, 213–224, doi:10.1016/j.pce.2004.01.008, 2004. 18756

Baldini, L. and Gorgucci, E.: Identification of the melting layer through dual-polarization radar measurements at vertical incidence, J. Atmos. Ocean. Tech., 23, 829–839, doi:10.1175/JTECH1884.1, 2006. 18750

Beard, K. V. and Chuang, C.: A new model for the equilibrium shape of raindrops, J. Atmos. Sci., 44, 1509–1524, 1987. 18761

Bech, J., Vilaclara, E., Pineda, N., Rigo, T., Lopez, J., O'Hora, F., Lorente, J., Sempere, D., and Fabregas, F. X.: The weather radar network of the Catalan Meteorological Service: description and applications, in: Proceedings of ERAD, vol. 2, 416–420, 2004. 18755

Black, R. A. and Hallett, J.: Rain rate and water content in hurricanes compared with summer rain in Miami, Florida, J. Appl. Meteorol. Clim., 51, 2218–2235, doi:10.1175/JAMC-D-11-0144.1, 2012. 18761

Blewitt, G.: Carrier phase ambiguity resolution for the Global Positioning System applied to geodetic baselines up to 2000 km, J. Geophys. Res., 94, 10187–10203, doi:10.1029/JB094iB08p10187, 1989. 18752

Bringi, V. N. and Chandrasekar, V.: Polarimetric Weather Radar; Principles and Applications, Cambridge University Press, 2001. 18750

Cardellach, E., Tomás, S., Oliveras, S., Padullés, R., Rius, A., de la Torre-Juárez, M., Turk, F. J., Ao, C. O., Kursinski, E. R., Schreiner, W., Ector, D., and Cucurull, L.: Sensitivity of PAZ LEO polarimetric GNSS radio-occultation experiment to precipitation events, IEEE T. Geosci. Remote, 53, 190–206, doi:10.1109/TGRS.2014.2320309, 2015. 18748, 18749, 18758, 18761, 18765, 18767

Cucurull, L. and Derber, J. C.: Operational implementation of COSMIC observations into NCEP's global data assimilation system, Weather Forecast., 23, 702–711, doi:10.1175/2008WAF2007070.1, 2008. 18748

Draine, B. T. and Flatau, P. J.: Discrete-dipole approximation for scattering calculations, J. Opt. Soc. Am. A, 11, 1491, doi:10.1364/JOSAA.11.001491, 1994. 18759

Draine, B. T. and Flatau, P. J.: User Guide for the Discrete Dipole Approximation Code DDSCAT 7.3, arXiv preprint, 3, available at: http://arxiv.org/abs/1305.6497 (last access: 06 July 2015), 2013. 18759

Ducrocq, V., Braud, I., Davolio, S., Ferretti, R., Flamant, C., Jansa, A., Kalthoff, N., Richard, E., Taupier-Letage, I., Ayral, P. A., Belamari, S., Berne, A., Borga, M., Boudevillain, B., Bock, O., Boichard, J. L., Bouin, M. N., Bousquet, O., Bouvier, C., Chiggiato, J., Cimini, D., Corsmeier, U., Coppola, L., Cocquerez, P., Defer, E., Delanoë, J., Di Girolamo, P., Doeren-becher, A., Drobinski, P., Dufournet, Y., Fourrié, N., Gourley, J. J., Labatut, L., Lambert, D., Le Coz, J., Marzano, F. S., Molinié, G., Montani, A., Nord, G., Nuret, M., Ramage, K., Ri-son, B., Roussot, O., Said, F., Schwarzenboeck, A., Testor, P., Van Baelen, J., Vincendon, B., Aran, M., and Tamayo, J.: HyMeX-SOP1, the field campaign dedicated to heavy precipitation and flash flooding in the northwestern Mediterranean, B. Am. Meteorol. Soc., 95, 1083–1100, doi:10.1175/BAMS-D-12-00244.1, 2014. 18749

Healy, S. B., Haase, J., and Lesne, O.: *Letter to the Editor* Abel transform inversion of radio oc-cultation measurements made with a receiver inside the Earth's atmosphere, Ann. Geophys., 20, 1253–1256, doi:10.5194/angeo-20-1253-2002, 2002. 18751, 18775

Healy, S. B., Jupp, A. M., and Marquardt, C.: Forecast impact experiment with GPS radio occul-tation measurements, Geophys. Res. Lett., 32, L03804, doi:10.1029/2004GL020806, 2005. 18748

Kennedy, P. C. and Rutledge, S. A.: S-band dual-polarization radar observations of winter storms, J. Appl. Meteorol. Clim., 50, 844–858, doi:10.1175/2010JAMC2558.1, 2011. 18750, 18762

Kursinski, E. R., Hajj, G. A., Schofield, J. T., Linfield, R. P., and Hardy, K. R.: Observing Earth's atmosphere with radio occultation measurements using the global positioning system, J. Geophys. Res., 102, 23429–23465, doi:10.1029/97JD01569, 1997. 18751

Liu, G.: A database of microwave single-scattering properties for nonspherical ice particles, B. Am. Meteorol. Soc., 89, 1563–1570, doi:10.1175/2008BAMS2486.1, 2008. 18761

Matrosov, S. Y.: Radar reflectivity in snowfall, IEEE T. Geosci. Remote, 30, 454–461, doi:10.1109/36.142923, 1992. 18750

Title Page

Abstract | Introduction

Conclusions | References

Tables | Figures

|◄ | ►|

◄ | ►

Back | Close

Full Screen / Esc

Printer-friendly Version

Interactive Discussion

Matrosov, S. Y. and Mace, G. G.: Observations of ice crystal habits with a scanning polarimetric W-band radar at slant linear depolarization ratio mode, J. Atmos. Ocean. Tech., 29, 989–1008, doi:10.1175/JTECH-D-11-00131.1, 2012. 18762

Noel, V. and Chepfer, H.: A global view of horizontally oriented crystals in ice clouds from Cloud-Aerosol Lidar and Infrared Pathfinder Satellite Observation (CALIPSO), J. Geophys. Res., 115, D00H23, doi:10.1029/2009JD012365, 2010. 18762, 18763

Rocken, C., Anthes, R., Exner, M., Hunt, D., Sokolovskiy, R., Ware, R. H., Gorbunov, M., Schreiner, W., Feng, D., Herman, B. M., Kuo, Y. H., and Zou, X.: Analysis and validation of GPS/MET data in the neutral atmosphere, J. Geophys. Res., 102, 2984–29866, doi:10.1029/97JD02400, 1997. 18748

Ryzhkov, A. V. and Zrnić, D. S.: Polarimetric method for ice water content determination, J. Appl. Meteorol., 37, 125–134, 1998. 18750

Smith, P. L.: Equivalent radar reflectivity factors for snow and ice particles, J. Clim. Appl. Meteorol., 23, 1258–1260, doi:10.1175/1520-0450(1984)023<1258:ERRFFS>2.0.CO;2, 1984. 18760

Steiner, A. K., Lackner, B. C., Ladstdter, F., Scherllin-Pirscher, B., Foelsche, U., and Kirchengast, G.: GPS radio occultation for climate monitoring and change detection, Radio Sci., 46, 1–17, doi:10.1029/2010RS004614, 2011. 18748

Trömel, S., Kumjian, M. R., Ryzhkov, A. V., Simmer, C., and Diederich, M.: Backscatter differential phase-estimation and variability, J. Appl. Meteorol. Clim., 52, 2529–2548, doi:10.1175/JAMC-D-13-0124.1, 2013. 18750

Ulbrich, C. W.: Natural variations in the analytical form of the raindrop size distribution, J. Clim. Appl. Meteorol., 22, 1764–1775, doi:10.1175/1520-0450(1983)022<1764:NVITAF>2.0.CO;2, 1983. 18760

Vivekanandan, J., Bringi, V. N., Hagen, M., and Meischner, P.: Polarimetric radar studies of atmospheric ice particles, IEEE T. Geosci. Remote, 32, 1–10, doi:10.1109/36.285183, 1994. 18750

Williams, C. R., Bringi, V. N., Carey, L. D., Chandrasekar, V., Gatlin, P. N., Haddad, Z. S., Meneghini, R., Joseph, M., S., Nesbitt, S. W., Petersen, W. A., Tanelli, S., Tokay, A., Wilson, A., and Wolff, D. B.: Describing the shape of raindrop size distributions using uncorrelated raindrop mass spectrum parameters, J. Appl. Meteorol. Clim., 53, 1282–1296, doi:10.1175/JAMC-D-13-076.1, 2014. 18760

Title Page

Abstract | Introduction

Conclusions | References

Tables | Figures

|◄ | ►|

◄ | ►

Back | Close

Full Screen / Esc

Printer-friendly Version

Interactive Discussion

Zhang, J., Crocker, N. A., Carter, T. A., Kubota, S., and Peebles, W. A.: Interaction between Faraday rotation and Cotton–Mouton effects in polarimetry modeling for NSTX, Rev. Sci. Instrum., 81, 3–6, doi:10.1063/1.3479042, 2010. 18754

Table 1. Summary of the relevant differences expected between the ROHP-PAZ spaceborne experiment and the conducted ground-based field campaign.

Ground-based experiment	ROHP-PAZ
Initial phase delay: unknown, need to subtract the mean value of each measured arc (Eq. 4)	Initial phase delay: calibrated from the polarimetric phase difference at highest layers of the atmosphere
Local multipath: multiple reflectors and environmental dependency because of dry/wet changes in electrical permittivity of soil and structures	Local multipath: expected stable properties of local satellite structure. No expected dependency on the environment
Thermodynamic profiles: Refractivity, pressure, temperature and humidity cannot be extracted	Thermodynamic profiles: Refractivity, pressure, temperature and humidity can be derived

Title Page

Abstract   Introduction

Conclusions   References

Tables   Figures

◄   ►

Back   Close

Full Screen / Esc

Printer-friendly Version

Interactive Discussion

Table 2. Summary of the standard deviation analysis, using different day sets. $\overline{\sigma_i}$ and N_i account for the mean standard deviation and the number of used days for each day set i.

PRN	$\overline{\sigma_{dry}}$ (mm)	N_{dry}	$\overline{\sigma_{wet}}$ (mm)	N_{wet}	$\overline{\sigma_{rain}}$ (mm)	N_{rain}
G10	2.706	20	2.895	112	3.992	25
G15	1.808	20	2.263	108	2.597	29
G22	2.565	20	3.167	113	3.738	24
G26	3.386	20	3.698	114	4.108	23
G31	1.809	20	1.876	113	2.584	24

Figure 1. Panoramic view from the observation site. The field of view is the area compressing azimuths from ∼ 160° (left) to ∼ 270° (right), looking south. Multiple metallic elements seen in the field of view, such as the meteorological station, the fence, the telecommunications antenna, etc. and others not pictured (metallic shelter, antenna supports ...) could affect the GNSS signal in the form of multipath.

Discussion Paper | Discussion Paper | Discussion Paper | Discussion Paper
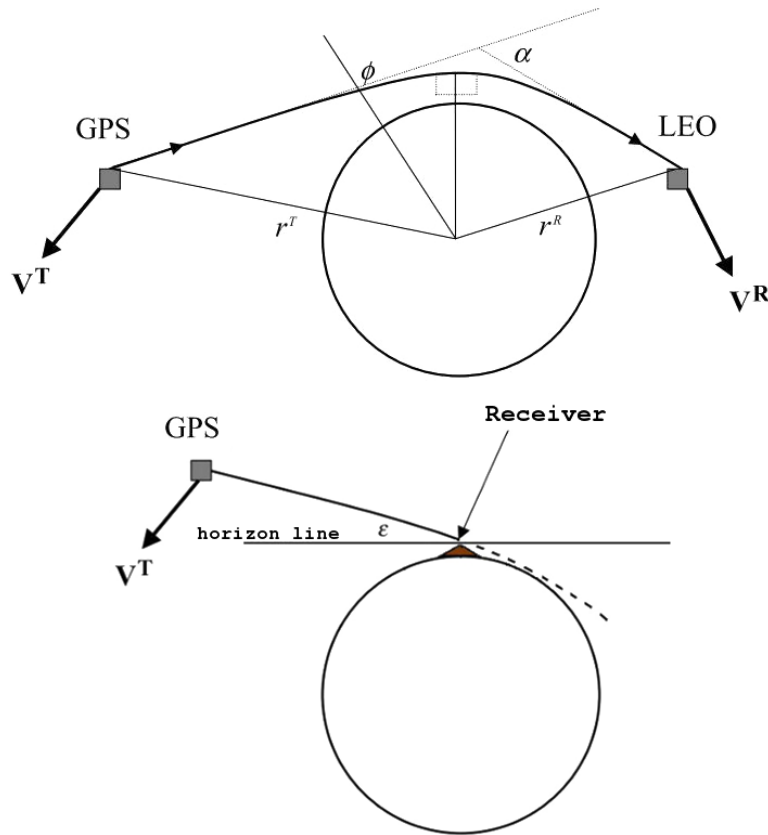
Figure 2. (top) Standard radio occultation geometry. (bottom) GPS-receiver radio link in a on ground receiver geometry, such as the one used in this experiment. ε accounts for elevation. Edited figure from original in Healy et al. (2002).
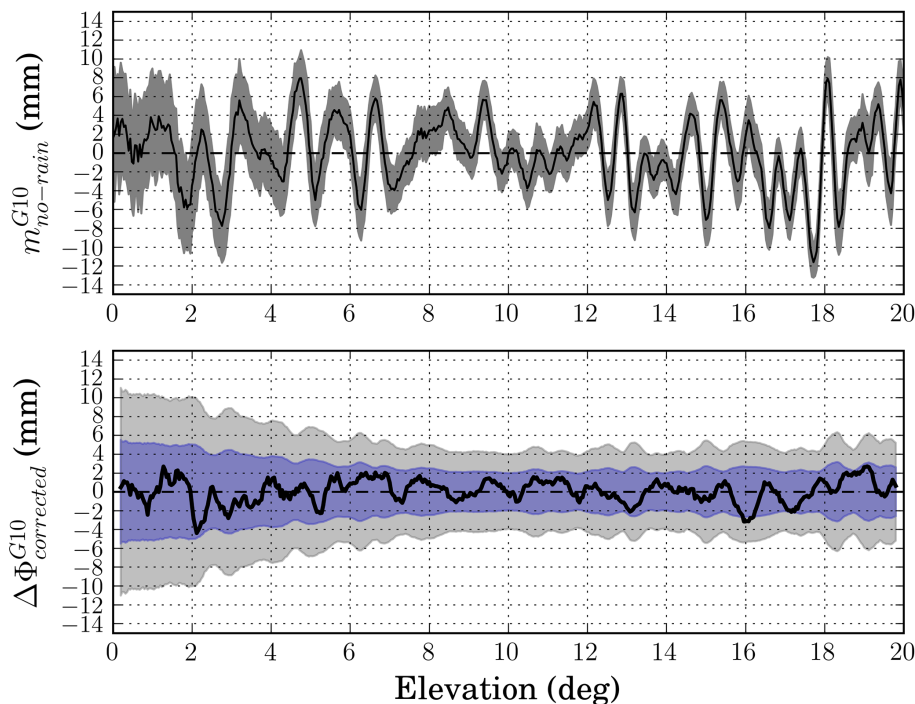
Figure 3. Examples of (top) multipath pattern after Eq. (4) for PRN 10 ($m_{no\text{-}rain}^{G10}$, $\sigma_{no\text{-}rain}^{G10}$), us-
ing a total of 132 days defined as *no-rain* days. Notice the large standard deviation at lower
elevations, and $\sigma_{no\text{-}rain}^{G10}$ of about 2 mm at higher elevations. (bottom) Corrected $\Delta\Phi_{day}^{PRN}(\epsilon)$ for
16 April 2014 (black line) after applying Eq. (5). The 1 and 2σ thresholds (multipath standard
deviation) are represented in blue and gray, respectively.

Title Page

Abstract | Introduction

Conclusions | References

Tables | Figures

◄ | ►

◄ | ►

Back | Close

Full Screen / Esc

Printer-friendly Version

Interactive Discussion
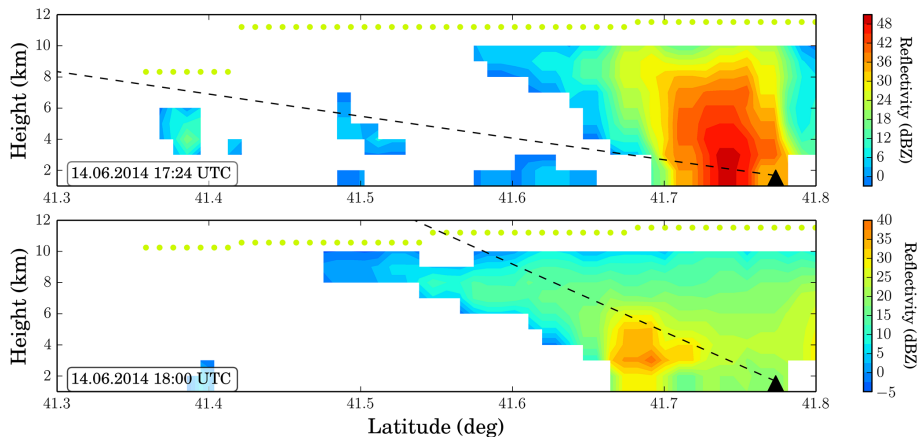
Figure 4. Illustration of the performed collocation at two different times of the same observation, a rising satellite link. A vertical slice of the radar reflectivity has been collocated with the Cloud top Phase (CP) product and the ray trajectory. The dashed black line is the projection of the ray trajectory as simulated with OAT ray tracer on the described plane, and the dots correspond to the CP. In this case, all the green dots indicate ice in the top of the clouds.
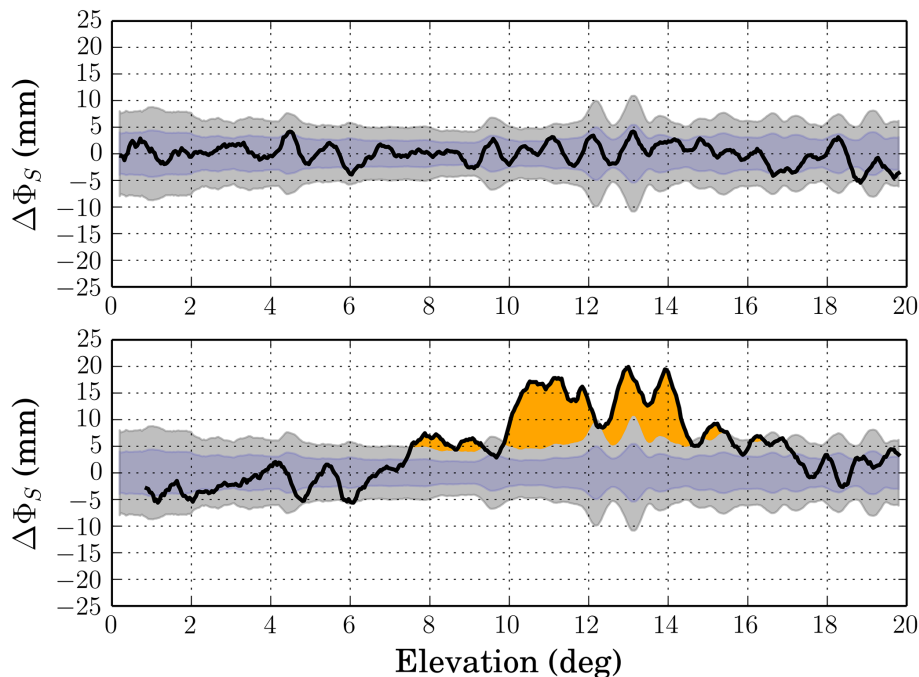
Figure 5. Examples of $\Delta\Phi_S(\epsilon)$ (black line), the $\pm\sigma_{\text{no-rain}}$ contour (blue) and the $\pm2\sigma_{\text{no-rain}}$ contour (gray), for two observations of the PRN G22 during 26 May 2014 (top) and 14 June 2014 (bottom). The top $\Delta\Phi_S(\epsilon)$ measurement is well inside the $2\,\sigma$ contour, showing no polarimetric signatures. On the bottom, case on 14 June 2014 shows large positive $\Delta\Phi_S(\epsilon)$. The value of $\Delta\Phi_S(\epsilon)$ above $2\sigma_{\text{no-rain}}$ threshold will be called hereafter $\Delta\Phi_+$, and its area (orange zone) A_Φ.

Title Page

Abstract | Introduction

Conclusions | References

Tables | Figures

|◄ | ►|

◄ | ►

Back | Close

Full Screen / Esc

Printer-friendly Version

Interactive Discussion
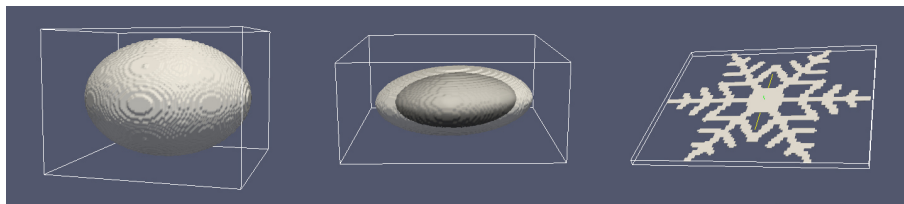
Figure 6. Target shapes used in DDScat. (left) Oblate ellipsoid, used to reproduce rain drops. (middle) Two concentric ellipsoids, used to simulated melting ice particles, with an ice core and a water shell. (right) Dendritic shape used to simulate the pristine ice particles.
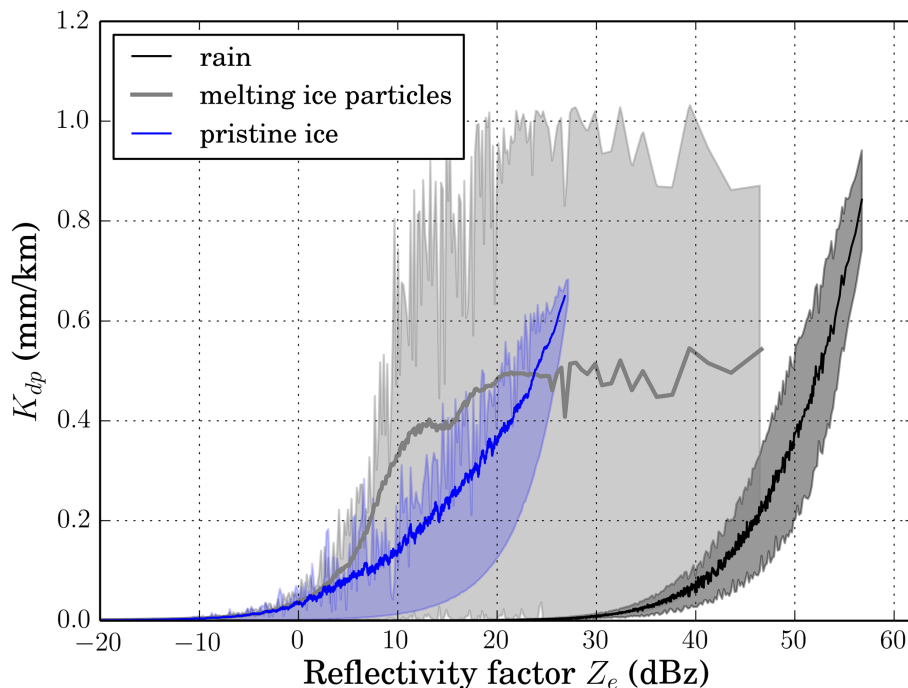
Figure 7. $K_{dp}(Z_e)$ for all the possible physically valid $N(D)$ for each hydrometheor type: rain (black), melting ice particles (gray) and ice crystals (blue). Rain drops need high reflectivity to produce high K_{dp}, while ice crystals and melting ice particles can induce high values of K_{dp} at smaller values of Z_e. The thick lines overplotted represent the Z_e–K_{dp} relation used in this analysis for each hydrometeor type.
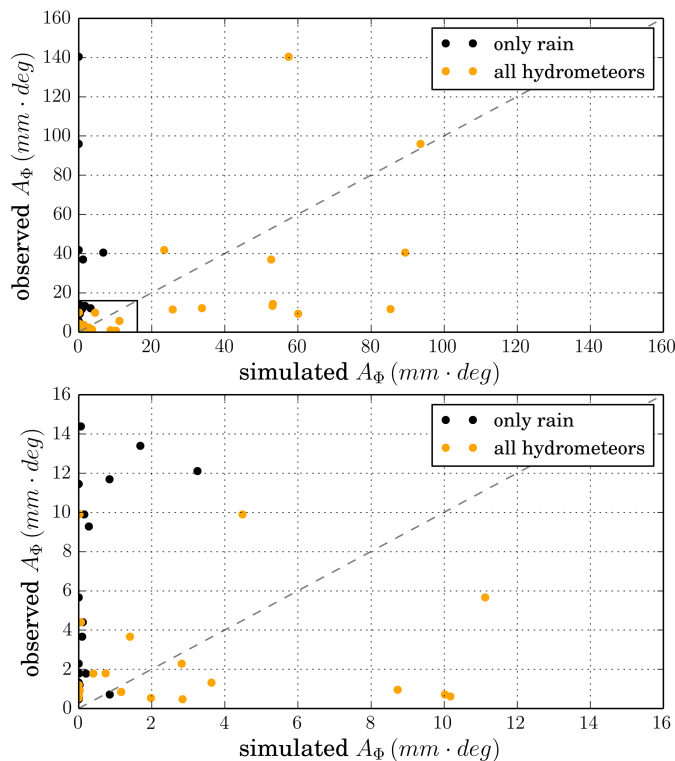
Figure 8. Observed vs. simulated A_Φ. A *zoom* of the lowest region in the bottom panel. Black dots represent the simulated A_Φ using only rain drops, while orange dots represent the simulated A_Φ accounting for ice crystals and melting ice particles too. The gray dashed line represents the perfect agreement between the observations and the modelling. The correlation coefficients for the data is $r = 0.60$, and it decreases to $r = 0.75$ when we take into account only the points with an observed $A_\Phi < 20$ mm·deg.
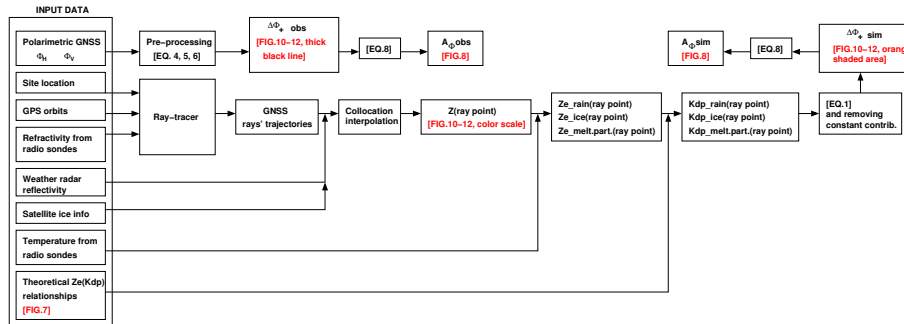
Figure 9. Block diagram showing all the data analysis and modelling process. Steps from the data aquisition to the final results are shown.

Printer-friendly Version

Interactive Discussion

Discussion Paper | Discussion Paper | Discussion Paper | Discussion Paper

ACPD

15, 18747–18785, 2015

ROHP-PAZ field campaign

R. Padullés et al.

Title Page

Abstract	Introduction
Conclusions	References
Tables	Figures

|◄   ►|

◄   ►

Back   Close

Full Screen / Esc

Printer-friendly Version

Interactive Discussion
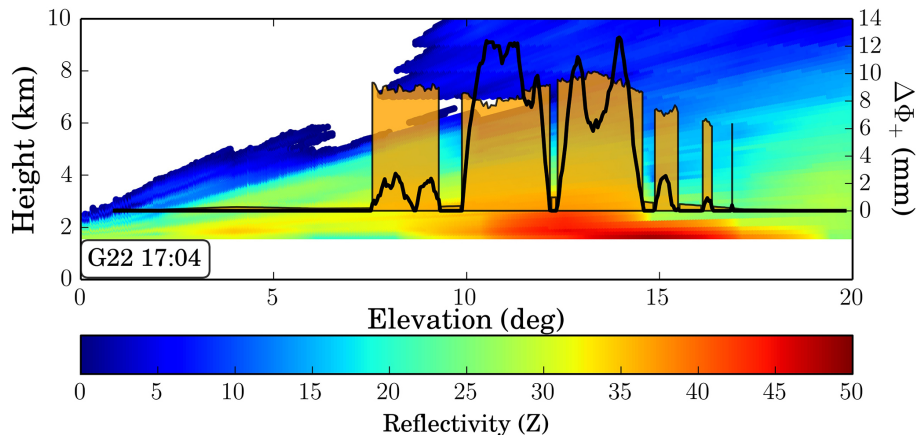
Figure 10. Each GNSS ray is identified by its elevation angle. Along a ray, each point can be identified by its height. The color scale shows the weather radar reflectivity Z_e interpolated along the GNSS rays. The black line is the $\Delta\Phi_+$ (right y axis). Simulation results performed as described in Sect. 5 are represented in orange shaded areas. In the regions where $\Delta\Phi_+ > 0$, all hydrometeors are taken into account in the simulations. Only rain is simulated otherwise.
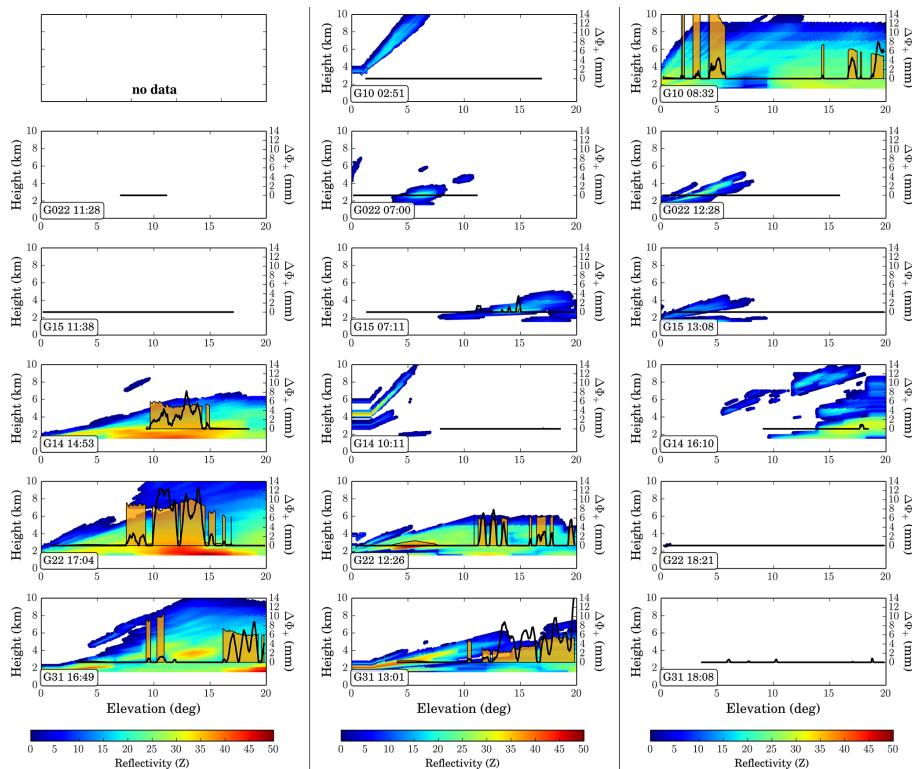
Figure 11. Rain episodes on 14 June 2014 (left), 22 August 2014 (middle) and 26 May 2014 (right). Each panel corresponds to a PRN, identified in the label on the lower left corner, along with the time of the observation start. Note that the radio-link with different PRNs corresponds to different time and also different azimuth. They are sorted in time, with the first one on the top. Content of each panel is explained in Fig. 10 caption.

Title Page

Abstract | Introduction

Conclusions | References

Tables | Figures

|◄ | ►|

◄ | ►

Back | Close
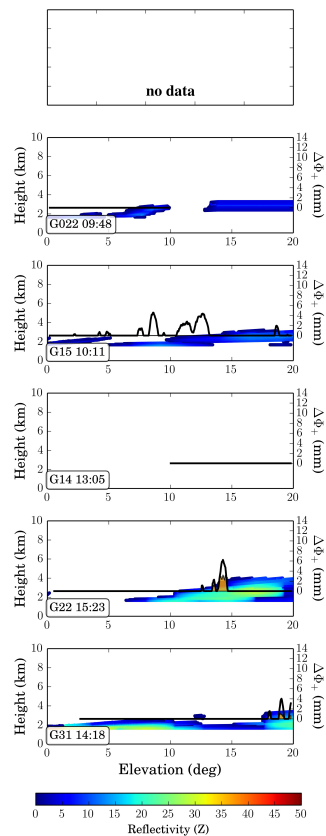
Full Screen / Esc

Figure 12. Same as Fig. 11, but for 09 July 2014. The signal in PRN G15 could not be explained with the used hydrometeors.